Physics of Fluids

Hydrodynamic performance of an unconstrained flapping swimmer with flexible fin: A numerical study

Cite as: Phys. Fluids **34**, 011901 (2022); https://doi.org/10.1063/5.0077312
Submitted: 01 November 2021 • Accepted: 10 December 2021 • Published Online: 04 January 2022

Buchen Wu (吴步晨), **Chang Shu** (舒昌), **Minping Wan** (万敏平), **et al.**

Physics of Fluids ARTICLE scitation.org/journal/phf

Hydrodynamic performance of an unconstrained flapping swimmer with flexible fin: A numerical study

Cite as: Phys. Fluids **34**, 011901 (2022); doi: 10.1063/5.0077312
Submitted: 1 November 2021 · Accepted: 10 December 2021 ·
Published Online: 4 January 2022

View Online Export Citation CrossMark

Buchen Wu (吴步晨),[1,2] Chang Shu (舒昌),[2,a)] Minping Wan (万敏平),[1,3,b)] Yan Wang (王岩),[4] and Shiyi Chen (陈十一)[1]

AFFILIATIONS

[1]Guangdong Provincial Key Laboratory of Turbulence Research and Applications, Department of Mechanics and Aerospace Engineering, Southern University of Science and Technology, Shenzhen, Guangdong 518055, China
[2]Department of Mechanical Engineering, National University of Singapore, 10 Kent Ridge Crescent, Singapore 119260, Singapore
[3]Guangdong-Hong Kong-Macao Joint Laboratory for Data-Driven Fluid Mechanics and Engineering Applications, Southern University of Science and Technology, Shenzhen 518055, China
[4]Department of Aerodynamics, Nanjing University of Aeronautics and Astronautics, Yudao Street 29, Nanjing, Jiangsu 210016, China

[a)]Electronic mail: mpeshuc@nus.edu.sg
[b)]Author to whom correspondence should be addressed: wanmp@sustech.edu.cn

ABSTRACT

Flexible tail fins are commonly found in undulatory swimmers which can propel freely in omni-direction with flapping-wing-based propulsion. In this work, the hydrodynamic performance of an unconstrained flapping foil equipped with a flexible tail fin at different length is investigated numerically. As the fin length L_{fin} changes from $0.2c$ to c with c being the cord length, the propelling speed of the system first increases and then decreases after maximum propelling speed is achieved when the fin length is $0.8c$. There are two kinds of wake vortical structures observed with bending stiffness $k_b = 2.0$: (i) the regular reverse Bénard–von Kármán vortex configuration for foil with short fin and (ii) the aligned vortices with two-layered street at downstream for foil with long fin ($L_{fin} \geq 0.6c$). Control volume analysis reveals that for both types of vortical structures, the time-averaged thrust force is mainly related to the momentum flux contribution from the downstream face. Besides, the wake symmetry of a pitching foil with flexible tail fin is sensitive to the vertical phase velocity of vortices, where it can be used to predict whether the wake symmetry of the unconstrained system is preserved. Moreover, the bending stiffness effectively affects the hydrodynamic performance, and the breaking of wake symmetry greatly reduces the propulsive efficiency. The results obtained shed some new light on the role of flexible structures in the self-propulsive biological system and furthered our understanding of flexible self-propulsion system.

I. INTRODUCTION

The propulsion mechanism of a biological flapping-wing system has received much attention recently due to the rapid development of autonomous underwater vehicles (AUVs) for modern subocean operations. Within the biological flapping-wing system, the flexible structures play one of the most important roles, for instance, the tail fin of a swimming fish, bacteria propulsion, and the wing flapping motion of birds. The flexible fin/wing of a self-propelled system often shows a considerable deformation during swimmer flapping motion,[1,2] which is passively controlled by the surrounding flow. The role of flexible structures in the self-propelled system always fascinates human, where extensive studies that have focused on the hydrodynamic performance of flexible structures have been carried out.[3–18] The flexible structures can enhance the performance of a tethered flapping system, such as promoting thrust generation[19,20] and increasing propulsive efficiency.[21–24] The biological flapping-wing system coupled with flexible structures is a general form of self-propelled system, where scientific investigation of such system can not only reveal the propulsion mechanisms of such system, but also be applied in designing bio-inspired propulsors.[25]

Several studies[3,4] have demonstrated that the flexible part of biological system can generate considerable advantage, i.e., high

propulsive efficiencies, than the rigid structures. It triggers many investigations onto the pitching foil with flexible flaps,[19–21,26–29] which can be regarded as the rigid part and flexible part of a biological system. These studies revealed that the flexibility can influence the flow field and the hydrodynamic forces of the rigid part. Heathcote and Gursul[21] reported that the propulsive efficiency is associated with the vortical strength of leading-edge vortex (LEV), Strouhal number (St), and pitching phase angle, where the optimal St and pitching phase angle to achieve peak efficiency are 0.125 and 95°–100° in angle, respectively. Dewey *et al.*[19] claimed that the pitching foil with flexible panel increases thrust generation and propulsive efficiency when compared to those with rigid panels. Besides, they found that there are two criteria required to achieve maximum propulsive in a system: (i) optimal range of the Strouhal number and (ii) the resonance between flapping frequency and natural frequency of the system. Shinde and Arakeri[26] investigated the flapping foil with flexible flap in the absence of a uniform inflow, revealing that the flexible flap is capable of suppressing the wake meandering and increasing the St with coherent orderly backward jet. In a subsequent work, they[27] revealed that the flexible structure can be divided into "*active portion*" and "*passive portion*." The momentum and kinetic energy of wake flow are enhanced by "*active portion*," while the "*passive portion*" dominants the position where the vortex sheds. It is worth mentioning here that LEVs are not found in the experiment work performed by Shinde and Arakeri,[27] but LEVs are reported in previous studies[30–32] to significantly enhance the trust. David *et al.*[20] discovered that the addition of a tethered rigid pitching foil with a flexible flap can further increase the efficiency by approximately three times when the dimensionless bending coefficient R^* is close to 0.01, and the peak thrust enhancement is achieved when $R^* \approx 8$. He *et al.*[33] investigated the effect of flexible flap on the aerodynamic force and flow structure of an airfoil at high angle of attack. They showed that the vibration amplitude Strouhal number St_A linearly increases with the Reynolds number and the wake width Strouhal number St_w was found to be in the range of 0.14–0.21, implying that the wake flow belongs to the bluff-body wake. Alaminos-Quesada and Fernandez-Feria[28] investigated an active deformed body followed by a flexible fin with a precribed deformation motion. Kurt *et al.*[29] studied the hydrodynamic performance of two staggered non-uniformly flexible foils at various arrangement, where they found that the efficiency and thrust are further enhanced with an increase in spacing ratio.

In nature, flapping-wing-based propulsive system can freely propel in omni-direction, but most studies that are available in literature placed their focus on the system composed of a tethered pitching foil with flexible flaps/panels, constraining it at a fixed position. Hence, despite a growing amount of works on system with a tethered pitching foil with flexible flaps/panels, these studies cannot accommodate all of the dynamic complexity of the real biology (flexible structure)-fluid interactions. There is little investigation on the hydrodynamic performance of self-propulsive unconstrained flapping foil with flexible tail fin, which can better mimic the characteristics of a true aquatic animal propulsion. In the present work, we investigate the hydrodynamic behaviors of a self-directed pitching foil with a flexible tail fin by varying the normalized length and dimensionless flexibility of the tail fin as these two parameters have important influences on the hydrodynamic forces and flow field.[19,20] In addition, the model (see Fig. 1) adopted in this study allows the pitching foil with flexible tail fin to freely propel in horizontal and vertical direction, allowing better representation of a true aquatic animal propulsion. This work aims to address the usefulness of a large passive deformation of flexible tail fin to self-propulsive hydrodynamic performances. The paper is organized as follows: the problem description and methodology are provided in Sec. II. Numerical results are presented and analyzed in Sec. III followed by conclusions in Sec. IV.

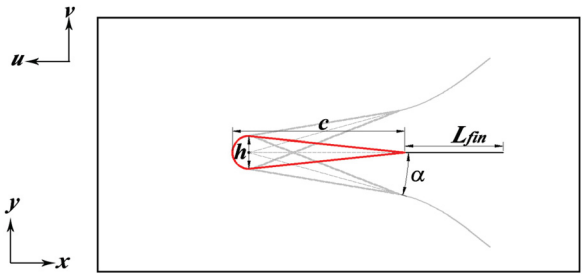

FIG. 1. Schematic view of the simplified model adopted. h is the thickness, c is chord length, L_{fin} is the length of flexible tail fin, and α is the instantaneous pitching motion.

II. PROBLEM DESCRIPTION AND METHODOLOGY

A. Simplified model

The animal body is simplified as a rigid foil with a semicircular leading edge, while the flexible fin is simplified as a two-dimensional flexible flag clamped at the foil end, as shown in Fig. 1. The computational domain is $75c \times 50c$ with Newmann boundary condition ($\partial \boldsymbol{u}/\partial n = 0$) being applied on all boundaries, where the region of $45c \times 10c$ is discretized by the uniform Cartesian grid with a mesh size of $\Delta x_{fluid} = 0.01c$. Here, c is the chord length. Besides, the flapping foil and the flexible fin are discretized by uniform Lagrangian points with the spacing of $\Delta x_{solid} = 0.015c$. The rigid foil pitches around the semicircular center with a simple harmonic pitching motion,

$$\alpha(t) = \alpha_m \sin(2\pi f t), \tag{1}$$

where $\alpha(t)$ is the instantaneous pitching angle, α_m is the pitching amplitude, and f is the pitching frequency.

B. Governing equation of flexible tail fin

The non-dimensional governing equation of motion[34,35] for a flexible fin with gravity force being neglected can be expressed as

$$\beta \frac{\partial^2 \boldsymbol{X}}{\partial t^2} = \frac{\partial}{\partial s}\left(\omega(s)\frac{\partial \boldsymbol{X}}{\partial s}\right) - \frac{\partial^2}{\partial s^2}\left(k_b \frac{\partial^2 \boldsymbol{X}}{\partial s^2}\right) + \boldsymbol{F}_H, \tag{2}$$

where β is the mass ratio between fin and fluid, and s is the Lagrangian coordinate along the flexible fin. $\boldsymbol{X}(s,t) = (x(s,t), y(s,t))$ is the position of Lagrangian points along the flexible fin, $\omega(s)$ is the non-dimensional tensile stress obtained from inextensibility constraint condition, k_b is the non-dimensional bending coefficient, and $\boldsymbol{F}_H$ is the non-dimensional hydrodynamic force applied on the flexible fin by the surrounding flow. Since the flexible fin is clamped on the foil end, the position $\boldsymbol{X}$, velocity $\boldsymbol{U}$, and the first derivative $\partial \boldsymbol{X}/\partial s$ of the fin's fixed end should be updated accordingly. The boundary conditions imposed on the flexible fin can be expressed as follows:

At fixed end,

$$\begin{cases} \boldsymbol{X} = \boldsymbol{X}_{foil\,end}, \\ \boldsymbol{U} = \boldsymbol{U}_{foil\,end}, \\ \dfrac{\partial \boldsymbol{X}}{\partial s} = (\cos\alpha(t),\ \sin\alpha(t)). \end{cases} \tag{3}$$

At free end,

$$\begin{cases} \dfrac{\partial^2 \boldsymbol{X}}{\partial s^2} = 0, \\ \dfrac{\partial^3 \boldsymbol{X}}{\partial s^3} = 0, \\ t(s) = 0. \end{cases} \tag{4}$$

The dimensionless parameters appearing in Eq. (2) are defined as follows: $k_b = B/(\rho_f U_{ref}^2 L_{fin}^3)$, $\omega(s) = \Omega(s)/(\rho_f U_{ref}^2 L_{fin})$, $\beta = \rho_s/(\rho_f L_{fin})$. Here, B, $\Omega(s)$, and ρ_s represent the dimensional bending stiffness, tension force, and linear density of the flexible tail fin, respectively. In this work, the mass ratio β is fixed at 1 to investigate the effect of fin length and bending stiffness on the propulsion of a freely flapping foil. The numerical method to solve the behavior of solid structure follows the previous work proposed by Ma *et al.*[35] Besides, the methodology for fluid-structure coupling follows previous studies, and details about the numerical process can be found in the literature.[35–39]

C. Governing equation of self-propulsion

As mentioned previously, the flapping foil is allowed to propel in the horizontal and vertical directions, where these motions can be described with the Newton's second law as follows:[40]

$$m\frac{d^2\boldsymbol{\Psi}}{dt^2} = \boldsymbol{F}, \tag{5}$$

where $\boldsymbol{\Psi}$ is the position of the flapping foil in both horizontal and vertical direction and $\boldsymbol{F}$ is the hydrodynamic force exerted on the foil surface by the ambient fluid. $m = \rho_{foil}A$ is the mass of the pitching foil, where ρ_{foil} is the area density of the foil and A is the area of the foil. Here, the area density of the foil is set equal to the fluid density as the mass ratio is not the focus of this work. The position and the propulsive speed of the solid system are obtained by adopting a trapezoidal rule and a forward differencing scheme, respectively, where they can be written as

$$\boldsymbol{X}^{t+\Delta t} = \boldsymbol{X}^t + \frac{\Delta t}{2}(\boldsymbol{u}^{t+\Delta t} + \boldsymbol{u}^t), \quad \boldsymbol{u}^{t+\Delta t} = \boldsymbol{u}^t + \frac{\boldsymbol{F}^t}{m}\Delta t, \tag{6}$$

where $\boldsymbol{u} = (u, v)$ is the propulsive speed of the system, and Δt denotes the time step. As shown in Fig. 1, the negative x direction is defined as the propulsive direction. Important characteristics of the system to quantify the self-propulsive performance such as (i) time-averaged horizontal propulsive speed and (ii) time-averaged vertical propulsive speed are computed as follows:

$$\bar{u} = \frac{1}{T}\int_0^T u dt, \quad \bar{v} = \frac{1}{T}\int_0^T v dt. \tag{7}$$

The propulsive efficiency of a system is the ratio of the averaged kinetic energy obtained from the pitching motion by foil ($\bar{E}_k$) to the averaged power consumption in one pitching period ($\bar{P}$), and it can be expressed as

$$\eta = \frac{\bar{E}_k}{\bar{P}T}, \tag{8}$$

where $\bar{P}$ is given as $\bar{P} = \frac{1}{T}\int_0^T (M(d\alpha/dt))dt$ and $\bar{E}_k$ is defined as $\bar{E}_k = \frac{1}{T}\int_0^T (\frac{1}{2}m(u^2 + v^2))dt$.

D. Governing equations

A lattice Boltzmann flux solver (LBFS)[41] for weakly compressible flow is adopted to simulate incompressible viscous flows. The mass and momentum conservation equations for incompressible flow are written as follows:

$$\nabla \cdot \mathbf{u} = 0, \tag{9a}$$

$$\frac{\partial \mathbf{u}}{\partial t} + \mathbf{u}\cdot\nabla\mathbf{u} = -\frac{1}{\rho_f}\nabla p + \nu\cdot\nabla^2\mathbf{u} + \boldsymbol{f}, \tag{9b}$$

where ρ_f is the fluid density, $\mathbf{u}$ is the flow velocity, ν is the kinematic viscosity, p is the pressure, and $\boldsymbol{f}$ is the forcing exerted by the solid system on the fluid. The interaction between the solid system and fluid is resolved by the explicit velocity correction based on the immersed boundary method.[42,43] More details on the numerical methods can be found in our previous works.[41–43]

E. Nondimensional parameters

The Reynolds number based on the characteristic velocity and chord length can be expressed as

$$Re = \frac{U_{ref}c}{\nu}, \tag{10}$$

where Reynolds number is kept constant at 200 in this study. In addition, the thickness-chord ratio (h/c) is kept constant at 0.1. The nondimensional length ($L = L_{fin}/c$) characterizing the length of the flexible fin varies between 0.2 and 1.0 in this work as this range covers most of the biological characteristics of available aquatic animals. Moreover, the length, time, propulsive speed, force, and vortex circulation are normalized by c, c/U_{ref}, U_{ref}, $\frac{1}{2}\rho_f U_{ref}^2 c$, and $U_{ref}c$, respectively. Since the physical properties of flexible tail fin is the main focus of this study, the dimensionless flapping parameters of $f = 2.0$ and $\alpha_m = \pi/18$ are employed. Table I shows the selected parameters employed in present work.

F. Validations

Code and numerical methods validation is carried out by repeating the work of Lin *et al.*[44] on the hydrodynamic performance of an unconstrained pitching foil (see Fig. 2), propelling in both horizontal

TABLE I. The specific values of the controlled parameters applied in current investigations.

Dimensionless parameters	Values
Normalized length L	0.2,0.4,0.6,0.8,1.0
Bending stiffness k_b	0.01,0.05,0.5,1.0,1.5,2.0,2.5,3.5,5.0

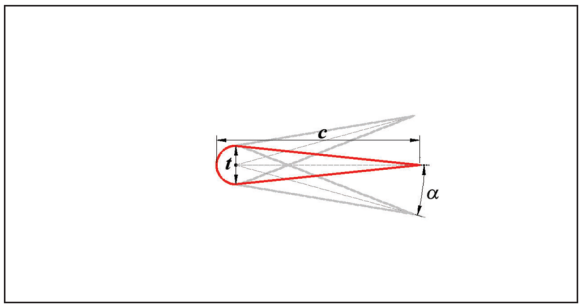

FIG. 2. Sketch view of an unconstrained pitching foil for validation.

and vertical directions in the absence of a uniform inflow. The parameters shown in Fig. 2 are the same as in the simplified model described in Sec. II A. Figure 3 shows that the results obtained from the present simulation methods agree well with the numerical results obtained in Lin *et al.*[44]

The numerical code is also rigorously tested for studying the deformability of the flexible structure under surrounding flow, where the numerical results were validated against experimental results.[45] As shown in Fig. 4, the present numerical results agree very well with the experimental data obtained by Kim *et al.*[45] in predicting the transverse displacement of the flag's free end.

III. RESULTS AND DISCUSSION

A. Effect of the normalized tail fin length

In this section, the effect of the tail fin length on the hydrodynamic performance of flapping-wing system is numerically investigated, where the tail fin length varies and the non-dimensional bending stiffness k_b is fixed.

1. Propulsive speed

First, the hydrodynamic performances of the foil with elastic tail fin and the foil with a rigid fin at various L are studied by comparing their propulsive speed, as shown in Table II. The cycle averaged horizontal speed is found to increase initially before decreasing as the fin length increases from 0.2 to 1.0. The peak cycle averaged horizontal

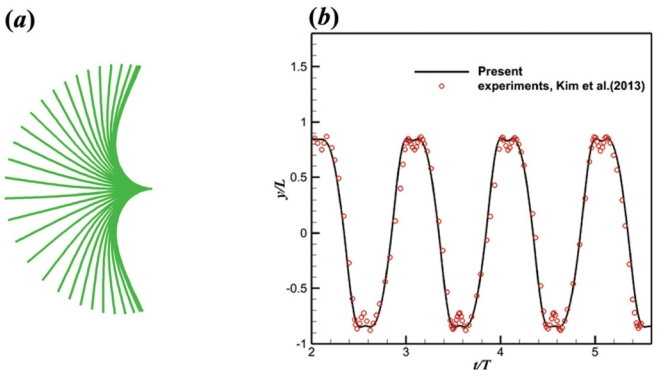

FIG. 4. (a) The flapping profile of inverted flapping flexible flag and (b) comparison of time histories of the transverse displacements of an inverted flexible flag in the case of (Re = 200, $k_b = 0.1$, $\rho = \rho_s/\rho_f L = 2.9$).

TABLE II. The cycle-averaged propulsive speed of foil with elastic fin and foil with rigid fin at various L. For bare foil, $\bar{u} = 0.31$ and $\bar{v} = 0$.

L		0.2	0.4	0.6	0.8	1.0
$\bar{u}$	Foil with rigid fin	0.55	0.94	1.23	1.55	1.61
	Foil with flexible fin	0.73	0.82	1.57	1.83	1.77
$\bar{v}$	Foil with rigid fin	0	−0.05	−0.08	−0.25	−0.30
	Foil with flexible fin	0	0.11	0	0	0

speed is found to occur at $L = 0.8$. In contrast to elastic tail fin, the $\bar{u}$ and $\bar{v}$ in foil with rigid fin tend to increase continuously with an increase in fin length, and it takes significantly more stokes to reach steady propulsion state than foil with flexible fin. It should be noted that $\bar{u}$ and $\bar{v}$ of the foil with rigid fin cannot reach a constant in present computational domain when $L > 0.6$; hence, the maximum cycle-averaged speed of those cases is given in Table II. More importantly, the horizontal speed of the foil with flexible fin is generally larger than the system with a rigid fin of the same length with the exceptional of $L = 0.4$, implying that the flexibility of tail fin is much more beneficial for the propulsion. The relatively low horizontal speed obtained for the flapping foil with elastic tail fin at $L = 0.4$ is partially attributed to the asymmetric wake structures, and they will be

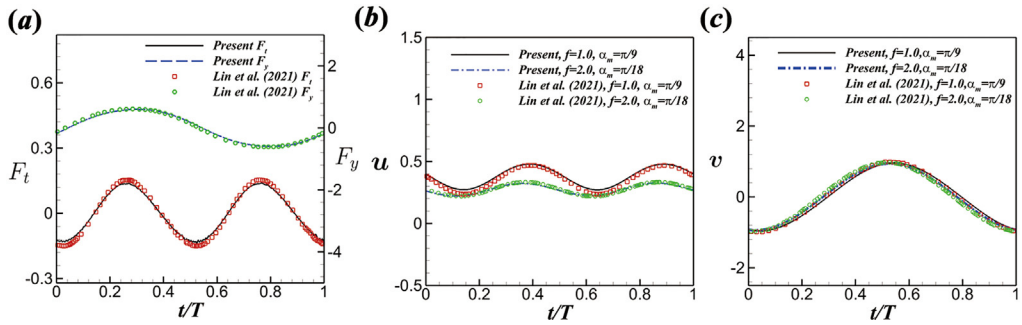

FIG. 3. Comparisons of time histories of (a) thrust and lift force of a single flapping foil in the case of (Re = 200, $f = 1.0$, $\alpha_m = \pi/9$), (b) horizontal propulsive speed, and (c) vertical propulsive speed of a single foil with various flapping parameters in the cases of (Re = 200, $f = 1.0$, $\alpha_m = \pi/9$ and Re = 200, $f = 2.0$, $\alpha_m = \pi/18$).

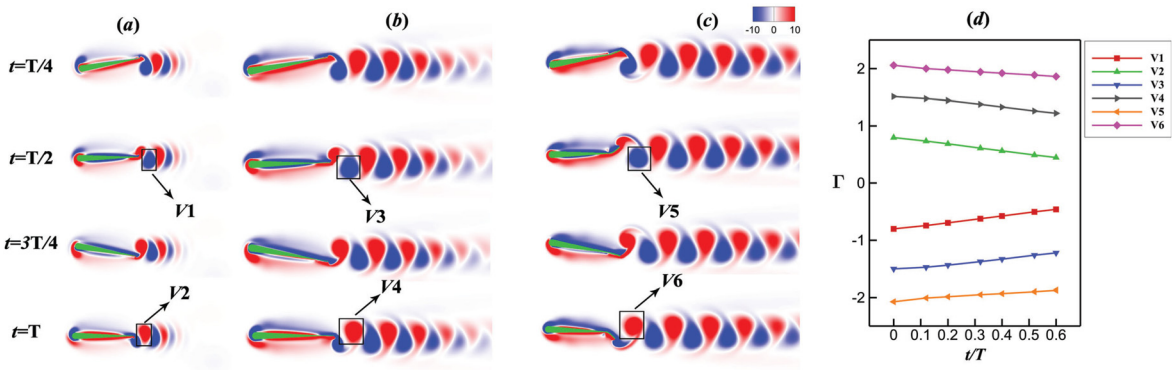

FIG. 5. The instantaneous vorticity contour for (a) the bare foil, (b) the foil with rigid fin at $L = 0.2$, and (c) the foil with flexible tail fin at $L = 0.2$. (d) The time evolutions of the circulations of the vortices shown in black frames of (a)–(c).

discussed in Sec. III A 3. Besides, the cycle-averaged vertical propulsive speed of the foil with elastic fin is zero for all fin length with the exceptional of $L = 0.4$. Also noteworthy is that the flexible fin is beneficial to preserve the wake symmetry, which can enhance the horizontal propulsive speed of the system and ensure the foil propels in straight direction. On the other hand, the system with rigid fins cannot effectively suppress the breaking of wake symmetry, and it also cannot keep a straight-line motion when $L > 0.2$.

2. Flow field

The wake vortex street of flapping foil with flexible tail at $L = 0.2$ is compared to bare foil and rigid tail fin to understand the role of flexible fin, as shown in Fig. 5. The vortex street of the foil with flexible tail fin is much longer compared to the other two systems and the vortex street of the foil with flexible fin dissipates more slowly than the rest. Besides, the foil with rigid fin generates larger vortices than the bare foil.

The time evolutions (a period of 0.6 T) of the vortex circulation ($\Gamma = \int\int_s \omega_z ds$) within the black square boxes shown in Figs. 5(a)–5(c) are shown in Fig. 5(d) to quantitatively determine the vortex strength by applying the Stokes' theorem. The size of the black box is chosen to be $6\sigma_x \times 6\sigma_y$, where σ_x and σ_y are obtained by using the Gaussian fit, $\exp(-x_i^2/\sigma_i^2)$. The center of the boxes is characterized by the maximum absolute value of vorticity. It is clear that the circulation of the foil with elastic tail fin is significantly larger than the other two systems. Besides, the strength of the vortices decreases with time due to the viscous dissipation occurred in all systems, and the absolute values of positive and negative circulations generated in the same cycle are almost identical. Figure 5(d) shows that the cycle-averaged horizontal propulsive speeds obtained from all cases are highly correlated with the vortical strength, echoing the finding from Zhang *et al.*[46] The animation of the pitching foil with flexible tail fin can be found in Fig. 6 (Multimedia view), where it shows the exceptional performance when compared to the other two systems.

To reveal the mechanism behind the hydrodynamic performance of the self-propelled foil with flexible tail fin, the wake properties of the system at various L are investigated. Figures 7 and 8 show the instantaneous vorticity contours and the time-averaged horizontal velocity contours of the system with flexible tail fin at various L, respectively. It is evident that the direction of the wake jet is associated with the vortex structures, and the symmetry breaking of the wave vortex street can either be inhibited or triggered, depending on the fin length L. At $L = 0.2$, the vortical strength of the wake is enhanced by the flexible fin, and a regular reverse Bénard–von Kármán (rBvK) is formed with a clear backward jet. At $L = 0.4$, the wake symmetry is preserved in the first 20 cycles [see Fig. 7(b)] before symmetry breaking of rBvK occurs [see Fig. 7(c)] and the strength of backward jet is enhanced. Therefore, the horizontal propulsive speed is enhanced based on the Newton's third law. At $L = 0.6$, the wake symmetry is preserved again and the vortices tend to be aligned at almost the same height, with rBvK almost disappearing. Surprisingly, a two-layered vortex street is formed in the wake downstream [see Fig. 8(d)], which prevents the aligned vortices from moving downstream. Such a two-layered vortex street is caused by the spacing ratio h/a between the wake vortices being greater than 0.365,[47,48] where h denotes the distance between the two vortex rows, and a is the spacing of the vortices with same sign. In addition, the unconstrained pitching foil with rigid tail fin only generates the rBvK vortex street with deflection backward jet at $L = 0.6$. At

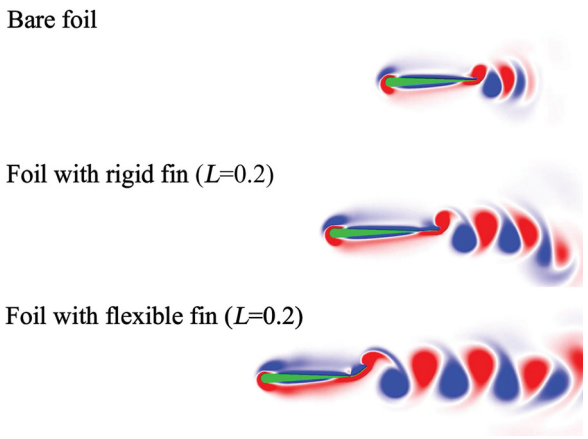

FIG. 6. The propulsive performance of the bare foil: the foil with rigid tail fin at $L = 0.2$ and the foil with flexible fin at $L = 0.2$. Multimedia view: https://doi.org/10.1063/5.0077312.1

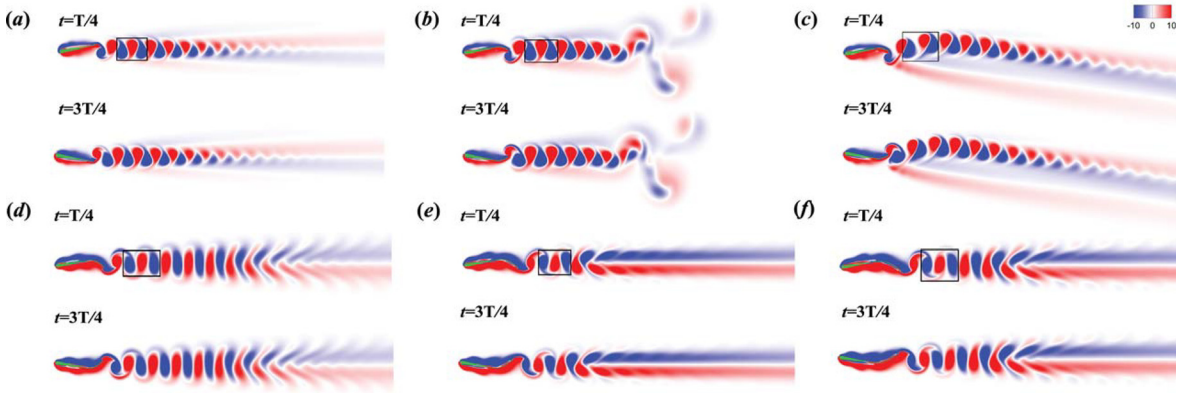

FIG. 7. The instantaneous vorticity contours (a)–(f) of system with flexible tail fin at various L at $t = 1/4T$ and $3/4T$: (a) denotes this system at $L = 0.2$, (b) is the symmetric stage of this system at $L = 0.4$, (c) presents the steady asymmetric stage of this at $L = 0.4$, and (d)–(f) show this system at $L = 0.6,0.8,1.0$, respectively.

$L = 0.8$, the vortical strength of the two-layered vortex street at wake downstream is further enhanced. At $L = 1.0$, the strength of the two-layered vortex street at wake downstream weakens and more aligned vortices exist between the system and two-layered vortex street; the horizontal propulsive speed is slightly lower than the system simulated at $L = 0.8$. It should be noted that, when the foil with flexible fin achieves steady propulsion, the time-averaged horizontal hydrodynamic force applied on the solid surface is zero.

The two layer vortex street at downstream of self-propelled system has not been reported or discovered in earlier works. One possible explanation on the lack of two layer vortex street observation is due to the tethered flapping-wing model employed in their work that constrained the rBvk vortex street to form only coherent backward jet. For instance, Shinde and Arakeri[26,27] discovered three kinds of backward jet in the absence of free stream flow, which are formed by the rBvK in the tethered flapping foil with flexible flap. David *et al.*[20] showed that the vortical strength of the rBvK configuration induced by the tethered pitching foil with flexible trailing edge flaps in a uniform flow dominates the thrust generation. To compare the hydrodynamic performance between unconstrained system and constrained system, the intrinsic properties of the constrained system at $L = 0.6$ and 0.8 are examined shown in Fig. 9. The comparison between the two systems shows the constrained system generates a rBvK vortex configuration with wake symmetry breaking and a deflected backward jet. It implies that the constrained system is prone to trigger the wake symmetry breaking, and the thrust is generated by the reaction force of the wake flow.

Moreover, Shinde and Arakeri[27] reported that the LEVs are not observed in their experiment, but our simulations clearly show that there are abundant vortex structures induced by the forward propulsion in the boundary layer around the pitching foil. In this sense, the tethered pitching foil has several limitations when it is used to investigate the effects of flexible structure on the flapping-wing-based propulsion, while the simplified model adopted here is capable of mimicking the real biological self-propulsion.

To investigate the influence induced by wake vortical structures at steady propulsive stage, we analyze the integral form of momentum equation for a moving, non-deforming control volume (CV) around the swimmer, as shown in Fig. 10. At any instant, the linear momentum equation for a moving CV with constant velocity can be written as

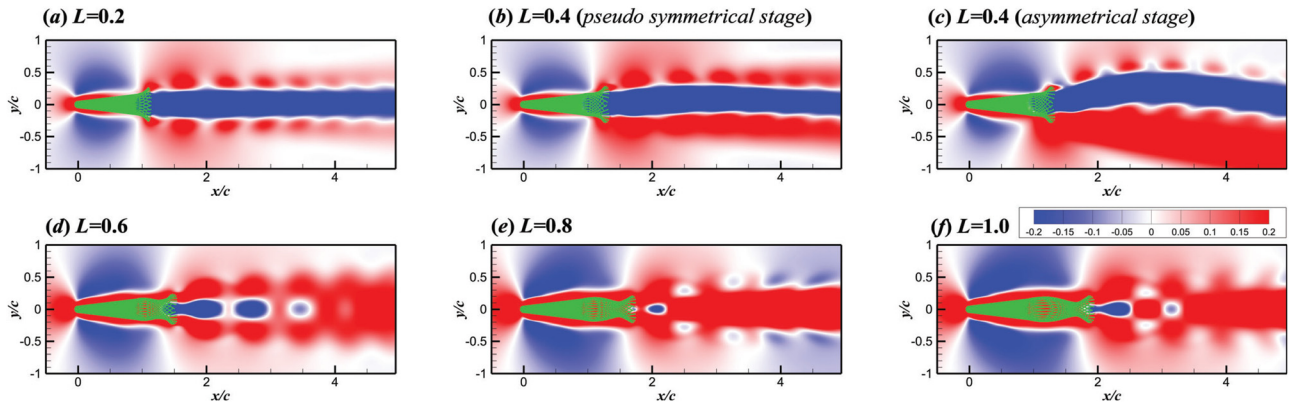

FIG. 8. The time-averaged horizontal velocity contours of system with flexible tail fin at various L. (a) denotes this system at $L = 0.2$, (b) is the symmetric stage of this system at $L = 0.4$, (c) presents the steady asymmetric stage of this at $L = 0.4$, and (d)–(f) show this system at $L = 0.6,0.8,1.0$, respectively. The green frame denotes the flapping profile in a pitching period.

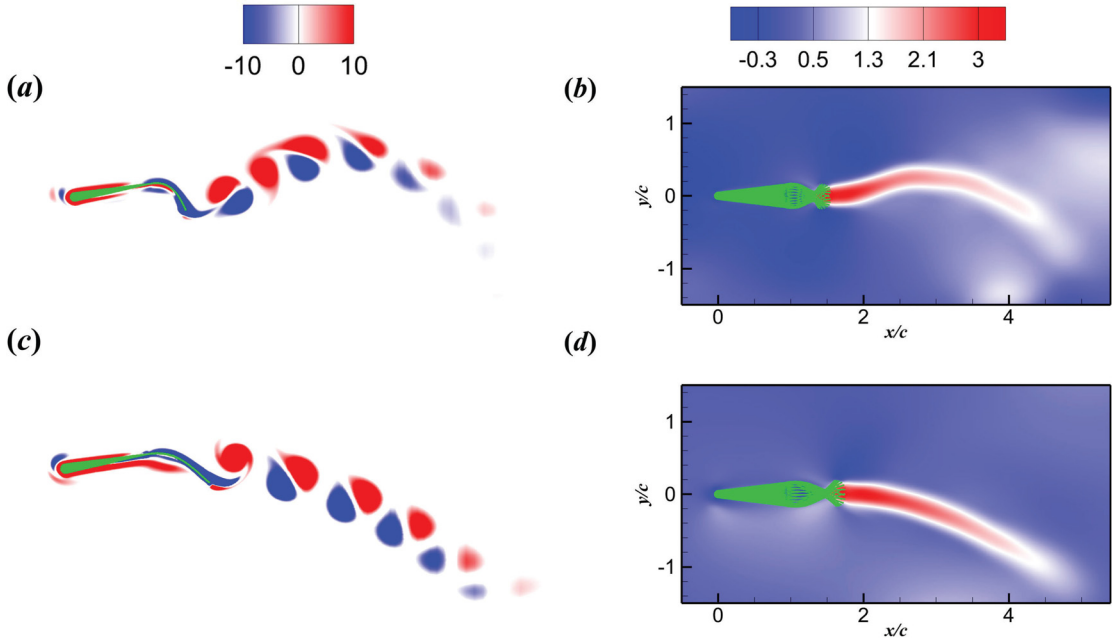

FIG. 9. (a) The instantaneous vorticity contours of the system (tethered pitching foil with flexible tail fin) at $L = 0.6$, (b) the time-averaged horizontal velocity contour of the system at $L = 0.6$, (c) the instantaneous vorticity contours of the system at $L = 0.8$, and (d) the time-averaged horizontal velocity contour of the system at $L = 0.8$. It should be noted that the positive x direction is defined as the velocity direction for the tethered cases.

$$\begin{cases} \dfrac{d}{dt}(m\mathbf{u})_{cv} = \dfrac{d}{dt}\displaystyle\int_{cs}\rho_f \mathbf{u} ds + \oint_l \rho_f \mathbf{u}(\mathbf{w}\cdot\mathbf{n})dl = \sum \boldsymbol{F}_{cv}, \\ \mathbf{u} = \mathbf{w} + \mathbf{u}_{cv}, \end{cases} \tag{11}$$

where $\mathbf{u}_{cv}$ denotes the velocity vector of the moving control volume. Hence, the streamwise momentum balance (the conservation of linear momentum law for a control volume) for this two-dimensional moving CV with constant velocity can be expressed as

$$\underbrace{\frac{d}{dt}\int_{cs}\rho_f u_f ds}_{\substack{\text{unsteady term} \\ \text{rate of momentum change}}} + \underbrace{\oint_l \rho_f u_f(\mathbf{w}\cdot\mathbf{n})dl}_{\substack{\text{momentum flux} \\ \text{flux term}}} = \underbrace{\sum F_x}_{\text{force term}}, \tag{12}$$

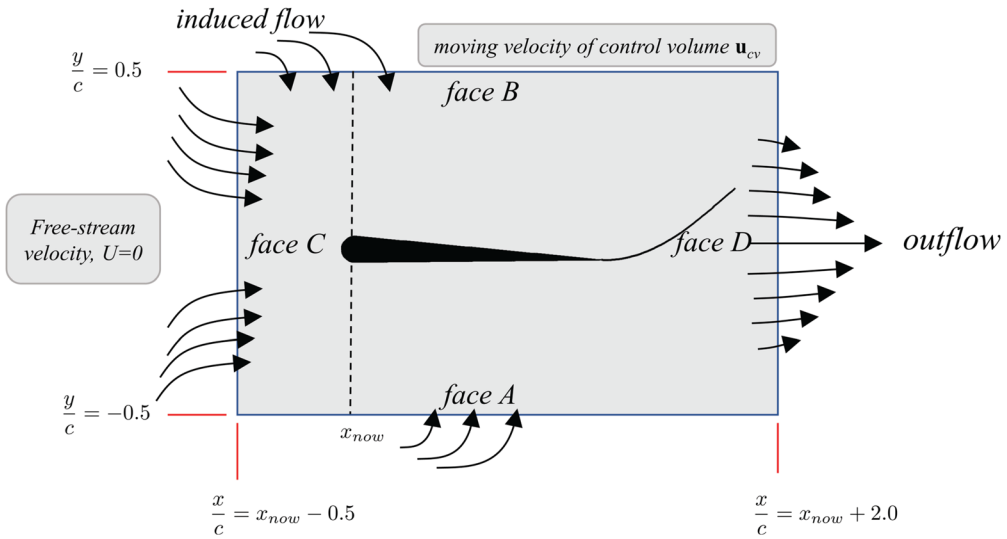

FIG. 10. Schematic view of the moving control volume around the swimmer at the initial time instant.

where u_f is the horizontal flow velocity, the first term denotes the rate of momentum change in the moving CV (the temporal derivative of the momentum content), and second term represents the momentum flux through its four control surfaces.

Here, the moving velocity of the CV is set as the time-averaged horizontal propulsive speed. We carried out the above CV analysis to the systems with fin length $L = 0.2$ and $L = 0.6$. Figure 11 shows the temporal variation of the three terms in Eq. (12) and the momentum flux contributions of four control surfaces, which clearly shows that two kinds of wake vortical structures induce different characteristics of momentum content and momentum flux variation. The time derivative of the momentum content in CV (the unsteady term) shows periodic variation with zero mean, indicating that the horizontal time-averaged force acting on the CV depends on the time-averaged momentum flux contribution through its four faces.

For the rBvK vortex configuration in the $L = 0.2$ case, the momentum flux on face D varies periodically, and its magnitude is significantly larger than the fluxes of other faces, with momentum fluxes at the other three faces close to zero. Meanwhile, for the aligned vortex configuration in the $L = 0.6$ case, the rate of momentum change and the momentum flux both fluctuates significantly. The total momentum flux is mainly contributed from the momentum flux of the downstream face D, with a small portion from upstream face C, while the contribution from the upper and lower face is almost zero. The total momentum flux contribution in the CV for the $L = 0.6$ case is larger than that of the system with $L = 0.2$, resulting that the net force applied on the CV is promoted. According to the Newton's third law, the thrust force of the flapping foil with flexible fin $L = 0.6$ is enhanced, promoting the propulsive speed.

3. Wake symmetry

As previously described, most of foils with elastic tail fin exhibit a zero cycle averaged vertical propulsive speed except for the case with $L = 0.4$, which produces a relatively large vertical speed and asymmetric wake structures with dipole vortices, as displayed in Fig. 7(c). Wake deflection of the flapping foil has been reported in previous studies,[49–54] and some criteria about the wake deflection are proposed. To better elucidate the mechanism of wake transition of this system, the vortex dynamic quantities at various L are examined. Considering the dipole vortex structures to appear, the two vortex pairs in the black frames (see Fig. 7) in a period of $0.6T$ are tracked. Here, the effective phase velocity is adopted to characterize the wake symmetry property, which can be obtained by the dipole model.[49] The dipole model is shown in Fig. 12, and the effective phase velocity U_p^* can be expressed as

$$U_p^* = U_{dipole} + U_{phase}\cos\beta, \tag{13}$$

where U_{phase} and V_{phase} are the averaged horizontal and vertical velocity of the two vortex centers, respectively. $U_{dipole} = \Gamma/(2\pi\xi)$ is the translation velocity of the dipole structure, in which Γ is the circulation of the dipole obtained by averaging the circulation value of the two vortices in the dipole in the yellow frame, as shown in Fig. 12. Following previous works,[49,50] the yellow frame sizes along the x and y directions are $2\sigma_x \times 2\sigma_y$, where σ_i $(i = x, y)$ is obtained by using the Gaussian fit, $\exp(-x_i^2/\sigma_i^2)$, and along x and y axes centered on the vortex center. β is the orientation angle between the direction of U_{dipole} and the horizontal direction. ϕ is the angle between vortex center lines. The wake vortical quantities of this system at various L are presented in Table III.

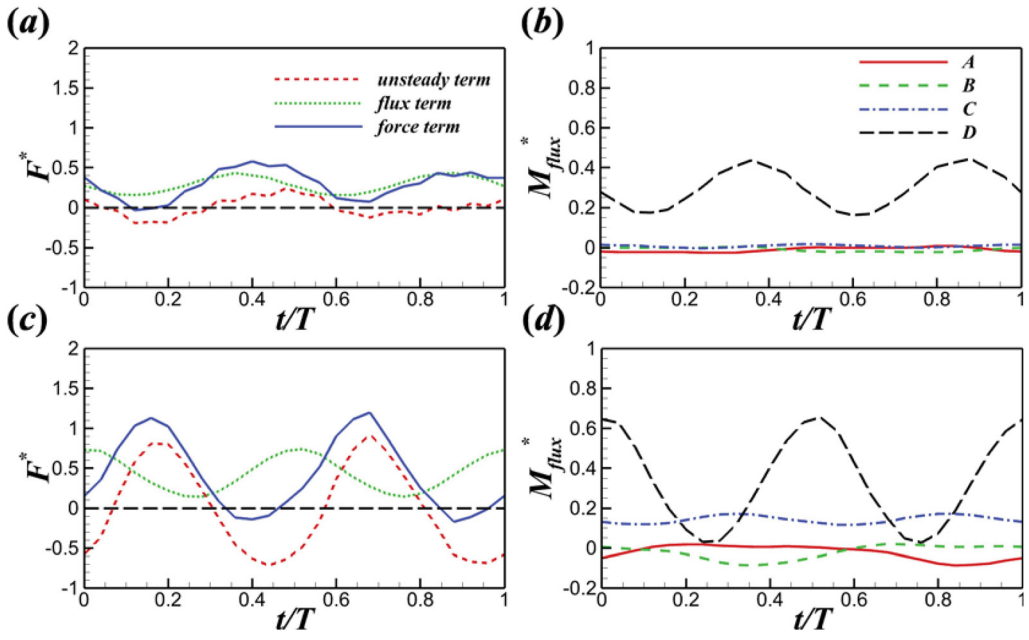

FIG. 11. (a) and (b) show the time-evolutions of the terms in Eq. (12) and the momentum flux contributions from CV four faces when $L = 0.2$, respectively; (c) and (d) show the time-evolutions of the terms in Eq. (12) and the momentum flux contributions from CV four faces when $L = 0.6$, respectively.

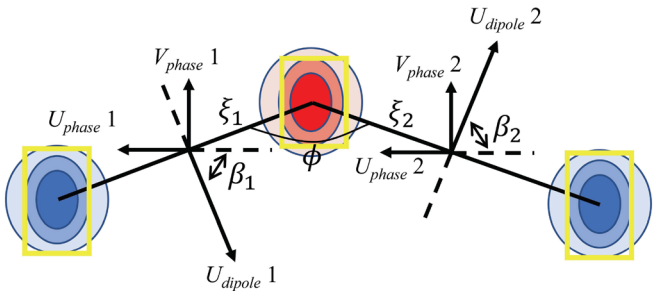

FIG. 12. A schematic illustration of two dipoles formed by the selected vortices.

A symmetry breaking condition ($U_p^* < 0$) was first proposed by Godoy-Diana *et al.*,[49] where subsequent work[50] found that wake will main symmetric if U_{p1}^* and U_{p2}^* in the dipole model are almost identical. In Table III, the difference between two effective phase velocities of this system, except at $L = 0.4$, is almost zero, which indicates that the wake symmetry will be preserved for these cases, as shown in Fig. 7. For the normalized tail fin length at $L = 0.4$, the difference between two effective phase velocities is quite large, and the dipole vortex structures emerge, which is consistent with the criterion.[50,52]

To better understand the reason behind the wake breaking found at $L = 0.4$, why the symmetry of the wake of this system at $L = 0.4$ is broken, the vortex dynamic quantities of wake vortex structures from symmetric stage to asymmetric stage are analyzed and tabulated as shown in Table IV. It should be noted that when $t/T = 10$, the circulations of two vortex pairs are 1.63 and 1.51, respectively, where they are larger than other cases. In addition, the difference increases as V_{phase} increases due to the circulation of the vortex pairs of this particular system at $L = 0.4$ is large, where small perturbation will enhance the difference between the two effective phase velocities. The importance of vertical phase velocity V_{phase} of vortex pairs in breaking the wake symmetry can be seen through the comparison of Tables III and IV, where the difference between vortex center is increased with an increase in V_{phase}, contributing to the breaking of wake symmetry.

Previous studies[50,52,55] have adopted the balance of two effective phase velocities to verify whether the wake symmetry is preserved. However, it is *a posteriori* model which only concentrates on the balance breaking and does not provide much information on the mechanism behind the destruction of the balance. Thus, previous dipole models are insufficient to predict the break of wake symmetry of the unconstrained system. In the present study, the detailed vortex dynamic quantities demonstrate that the vertical phase velocity V_{phase} of vortex pairs is an important indicator in predicting whether the wake symmetry of the unconstrained system will be broken, even in a pseudo symmetric state where the two effective phase velocities U_p^* are almost identical. The critical value of vertical phase velocity V_{phase} inducing the wake symmetry breaking warrants further investigations.

B. Effect of the bending stiffness

In this section, the effect of the bending stiffness on the hydrodynamic performance of a pitching foil with flexible tail fin is studied, and a fixed normalized fin length $L = 0.6$ is adopted.

1. Propulsive properties

The cycle-averaged horizontal propulsive speed $\bar{u}$, cycle-averaged vertical speed $\bar{v}$, averaged normalized power consumption $\bar{P}$, and normalized propulsive efficiency η of the pitching foil with elastic fin at different bending stiffness k_b are shown in Fig. 13, indicating that the hydrodynamic performance is affected by the flexibility of tail fin.

As the k_b is in the range of 0.5–2.5, the horizontal propulsive speed $\bar{u}$ and the power consumption $\bar{P}$ showed a downward trend

TABLE III. The values of physical quantities of vortices for foil with flexible tail fin at various L. U_{p1}^*, U_{p2}^*, U_{phase1}, U_{phase2}, V_{phase1}, and V_{phase2} denote the effective phase velocities and horizontal and vertical phase velocities of two dipoles, respectively.

L	U_{p1}^*	U_{p2}^*	Γ_1	Γ_2	U_{phase1}	U_{phase2}	V_{phase1}	V_{phase2}	ξ_1	ξ_2	ϕ (deg.)
0.2	0.42	0.40	1.33	1.20	−0.29	−0.25	0	0	0.38	0.36	119.89
0.4	0.23	0.46	1.55	1.26	−0.38	−0.33	0.38	0.33	0.56	0.33	119.24
0.6	0.53	0.51	1.36	1.29	0	0	0	−0.04	0.41	0.40	151.26
0.8	0.49	0.52	1.17	1.13	0.13	0.21	−0.04	0	0.40	0.38	205.30
1.0	0.49	0.48	1.29	1.24	0.04	0.13	0	0.04	0.42	0.41	180.00

TABLE IV. The values of vortex dynamic quantities of foil with flexible tail fin at $L = 0.4$ in different stages.

t/T	U_{p1}^*	U_{p2}^*	Γ_1	Γ_2	U_{phase1}	U_{phase2}	V_{phase1}	V_{phase2}	ξ_1	ξ_2	ϕ (deg.)
10	0.49	0.49	1.63	1.51	−0.29	−0.25	0.04	0	0.41	0.38	119.73
15	0.50	0.51	1.69	1.49	−0.29	−0.25	0	0.04	0.42	0.37	120.91
20	0.47	0.51	1.67	1.51	−0.29	−0.29	0.12	0.12	0.43	0.36	119.90
30	0.36	0.47	1.62	1.35	−0.25	−0.38	0.13	0.13	0.52	0.33	117.11
40	0.31	0.52	1.56	1.27	−0.25	−0.25	0.25	0.13	0.56	0.32	119.27
50	0.23	0.46	1.55	1.26	−0.38	−0.33	0.38	0.33	0.56	0.33	119.24

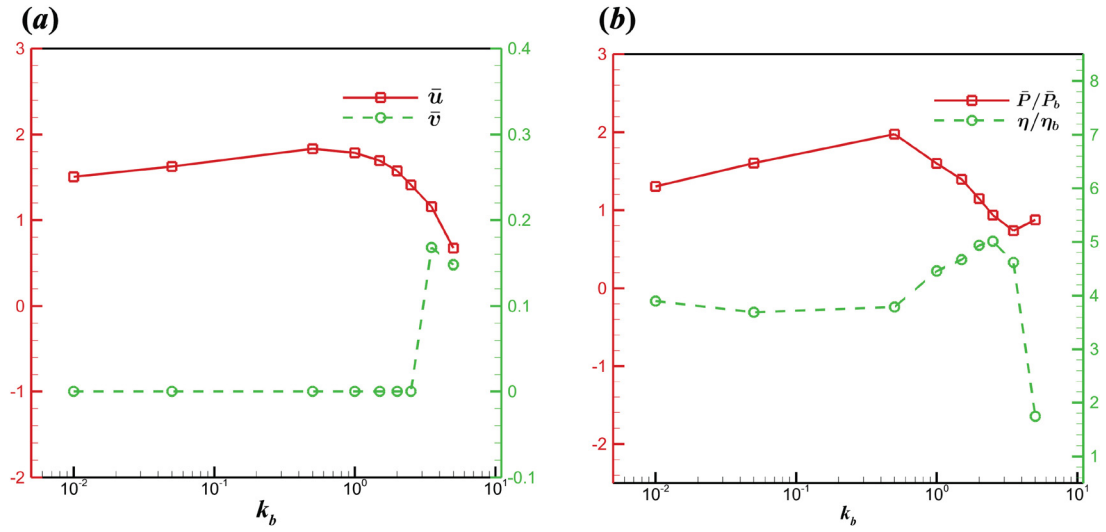

FIG. 13. The value of (a) cycle-averaged horizontal velocity $\bar{u}$, cycle-averaged vertical velocity $\bar{v}$, (b) averaged normalized power consumption $\bar{P}/\bar{P}_b$, and averaged normalized propulsive efficiency η/η_b of the unconstrained pitching foil with flexible tail fin at different flexibility k_b, where $\bar{P}_b$ and η_b denote the power consumption and propulsive efficiency of bare pitching foil at steady propulsion, respectively.

with a zero vertical propulsive speed $\bar{v}$, where the system propels forward with a steady symmetric motion. These observations show that the power consumption is proportional to the horizontal propulsive speed when the wake symmetry is preserved. However, the propulsive efficiency η shows an upward tendency and the optimal propulsive efficiency is achieved at $k_b = 2.5$, indicating that the increase in bending stiffness k_b is conducive to converting power into kinetic energy for bending stiffness at this range. It should be noted that David *et al.*[20] found that the optimal propulsive efficient is achieved at $k_b = 0.01$ for the tethered foil with flexible trailing edge flaps. The difference may be contributed by the fact that the system investigated here is not a tethered system and also that different flapping parameters and normalized fin length are adopted in this study.

When the bending stiffness $k_b > 2.5$, the breaking of wake symmetry is triggered and the cycle-averaged vertical propulsive speed $\bar{v}$ increases. As shown in Fig. 13(a), the decreasing rate of cycle-averaged horizontal propulsive speed is strengthened as the tail fin becomes more rigid. Although the cycle-averaged vertical propulsive speed has increased, the horizontal propulsive speed is still the dominant component in the kinetic energy. Besides, an important characteristic is the anti-correlation between propulsion speed and power consumption, where low propulsive speed does not represent less power input. Moreover, with the increase in bending stiffness, the propulsive efficiency decreases significantly when the wake symmetry is broken. The propulsion efficiency of a rigid tail fin tends to be closer to that of the bare pitching foil.

2. Wake structure

The vorticity contours and the time-averaged horizontal velocity contours at different flexibility k_b are shown in Fig. 14, showing that the wake vortex street is sensitive to the bending stiffness of tail fin. At small bending stiffness ($k_b = 0.5$), the vortices shedding from the tail fin form a short two-layered vortex street, which is very unstable and transits rapidly into secondary vortices. This phenomenon is similar to the secondary vortex formation in a circular cylinder wake at $\mathrm{Re} = 200$,[56] which is triggered by the convective instability of the shear layers.

With the increase in bending stiffness, the two-layered vortex street tends to be stable and the formation of secondary vortices is suppressed at $k_b = 1.0$–2.0. Besides, the number of the aligned vortices between the flexible trailing edge and two-layered vortex street also increases. An interesting phenomenon is that reducing the bending stiffness can achieve a similar vortex pattern generated by increasing the tail fin length.

When the bending stiffness is further increased, an important characteristic of wake vortex structure is that the two-layered vortex street disappeared, and the regular rBvk is recovered again when $k_b = 2.5$. When the bending stiffness is very large, e.g., $k_b = 5.0$, the dipole vortex structures are observed and the deflected coherent backward jet appears. With the large passive vertical flapping amplitude of trailing edge, the cycle-averaged vertical propulsive speed is induced, which is associated with the breaking of wake symmetry and leads to the vertical drift. Further examination on the vortex dynamic quantities reveals that the vortex dynamic quantities show that the increase in vertical phase velocity is the initial trigger to break the wake symmetry, as discussed in Sec. III A 3.

IV. CONCLUSIONS

In summary, the propulsive performance and vortex structures of an unconstrained foil with flexible tail fin are numerically investigated, where the effect of tail fin length as well as the effect of its bending stiffness is examined.

At an intermediate bending stiffness $k_b = 2.0$, the effect of tail fin length is investigated. The foil with flexible tail fin achieves a larger propulsive speed than the foil with rigid tail fin when the wake symmetry is preserved. As the fin length increases from $L = 0.2$ to $L = 1.0$, the horizontal propulsive speed of the pitching foil with tail fin

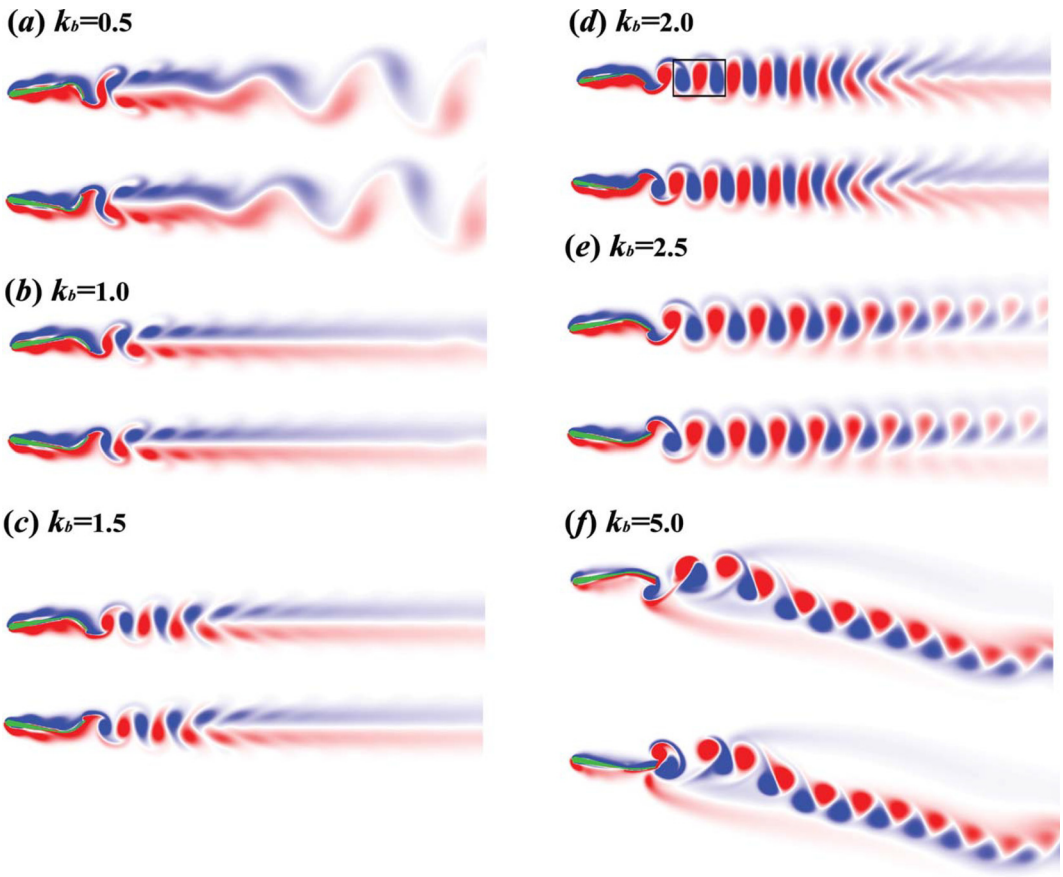

FIG. 14. The instantaneous vorticity contours (a)–(f) of the unconstrained pitching foil with tail fin at various flexibilities k_b when flapping foil changes the rotational direction.

increases initially and decreases subsequently with the maximum propulsive speed achieved when $L = 0.8$. There are two kinds of vortex streets observed: for short fin ($L \leq 0.4$), the regular rBvK vortex street and (ii) for long fin ($L \geq 0.6$), the aligned vortices with two-layered street at downstream. The CV analysis shows that for both two wake vortex configurations, the time-averaged thrust generation mainly depends on the momentum flux contribution from the downstream face.

Besides, with the increase in tail fin length, the switching of two vortex configurations is triggered. In contrast to the pitching foil with a rigid tail fin, the wake symmetry of the flapping foil with flexible tail fin is well preserved for different tail lengths except for the case with $L = 0.4$, where its wake symmetry is broken and a vertical component of propulsive velocity is produced. Detailed quantitative analysis reveals that the increase in vertical phase velocity V_{phase} is the initial disturbance to break the balance of two effective phase velocity U_p^*; thus, the vertical phase velocity V_{phase} is an effective indicator to predict whether the wake symmetry of the unconstrained flapping-wing system could be preserved.

At a fixed normalized tail fin length $L = 0.6$, the effect of bending stiffness of tail fin is studied. The propulsive performance of the system can be divided into three regions. At small bending stiffness $k_b \leq 0.5$, with the increase in bending stiffness enhancing the flapping velocity of trailing edge, the propulsive speed is promoted. At intermediate bending stiffness $k_b = 0.5$–2.5, the switching of two wake vortex configurations is triggered at $k_b = 2.5$ and the optimal propulsive efficiency is achieved at $k_b = 2.5$. At large bending stiffness $k_b > 2.5$, the wake symmetry breaking is triggered and the propulsive efficiency decreases. Besides, the declining rate of the propulsive efficiency is enhanced with more rigid tail fin. For symmetric propulsion, the cycle-averaged vertical propulsive speed remains at zero, and there is a positive correlation between the power consumption and the cycle-averaged horizontal propulsive speed $\bar{u}$. For asymmetric propulsion, the cycle-averaged vertical propulsive speed is induced and the propulsive efficiency rapidly declines, indicating that the asymmetric propulsion with vertical drift is inefficient.

A limitation of the present work is that the flapping-wing system with flexible tail fin is investigated at $\mathrm{Re} = 200$ in two dimensions based on some specific parameters. More works are required to include important effects such as the shape of the swimmer, the three-dimensional geometry, the distribution of bending stiffness, other propulsive parameters, and different Reynolds numbers to better mimic the realistic biology system.

ACKNOWLEDGMENTS

This work has been supported by the National Numerical Wind Tunnel Project (No. NNW2019ZT1-A01), NSFC (Grant No. 91752201), Shenzhen Science & Technology Program (Grant No. KQTD20180411143441009) and the Department of Science and Technology of Guangdong Province (Grant Nos. 2019B21203001 and 2020B1212030001). Numerical simulations have been supported by the Center for Computational Science and Engineering of Southern University of Science and Technology. B.W. would like to acknowledge and thank Dr. Fangbao Tian for his kind assistance.

AUTHOR DECLARATIONS

Conflict of Interest

The authors have no conflicts to disclose.

DATA AVAILABILITY

The data that support the findings of this study are available from the corresponding author upon reasonable request.

REFERENCES

[1]S. Combes and T. Daniel, "Flexural stiffness in insect wings I. Scaling and the influence of wing venation," J. Exp. Biol. **206**, 2979–2987 (2003).
[2]S. Combes and T. Daniel, "Flexural stiffness in insect wings II. Spatial distribution and dynamic wing bending," J. Exp. Biol. **206**, 2989–2997 (2003).
[3]T. Y.-T. Wu, "Hydromechanics of swimming propulsion. Part 1. Swimming of a two-dimensional flexible plate at variable forward speeds in an inviscid fluid," J. Fluid Mech. **46**, 337–355 (1971).
[4]J. Katz and D. Weihs, "Hydrodynamic propulsion by large amplitude oscillation of an airfoil with chordwise flexibility," J. Fluid Mech. **88**, 485–497 (1978).
[5]K. Sekimoto, N. Mori, K. Tawada, and Y. Y. Toyoshima, "Symmetry breaking instabilities of an in vitro biological system," Phys. Rev. Lett. **75**, 172 (1995).
[6]Q. Zhu, "Numerical simulation of a flapping foil with chordwise or spanwise flexibility," AIAA J. **45**, 2448–2457 (2007).
[7]H. Dai, H. Luo, P. J. F. de Sousa, and J. F. Doyle, "Thrust performance of a flexible low-aspect-ratio pitching plate," Phys. Fluids **24**, 101903 (2012).
[8]N. Moore, "Analytical results on the role of flexibility in flapping propulsion," J. Fluid Mech. **757**, 599 (2014).
[9]S. Michelin and S. G. Llewellyn Smith, "Resonance and propulsion performance of a heaving flexible wing," Phys. Fluids **21**, 071902 (2009).
[10]F. Paraz, L. Schouveiler, and C. Eloy, "Thrust generation by a heaving flexible foil: Resonance, nonlinearities, and optimality," Phys. Fluids **28**, 011903 (2016).
[11]Z. Peng, H. Huang, and X. Lu, "Hydrodynamic schooling of multiple self-propelled flapping plates," J. Fluid Mech. **853**, 587–600 (2018).
[12]G. Shi, Q. Xiao, and Q. Zhu, "Effects of time-varying flexibility on the propulsion performance of a flapping foil," Phys. Fluids **32**, 121904 (2020).
[13]L. Cong, B. Teng, and L. Cheng, "Hydrodynamic behavior of two-dimensional tandem-arranged flapping flexible foils in uniform flow," Phys. Fluids **32**, 021903 (2020).
[14]Z. Liu, F. Qin, L. Zhu, R. Yang, and X. Luo, "Effects of the intrinsic curvature of elastic filaments on the propulsion of a flagellated microrobot," Phys. Fluids **32**, 041902 (2020).
[15]M. Furquan and S. Mittal, "Flow-induced vibration of filaments attached to two side-by-side cylinders," Phys. Fluids **33**, 063609 (2021).
[16]A. Sankaran, S. Pawłowska, F. Pierini, T. Kowalewski, and A. Yarin, "Dynamics of electrospun hydrogel filaments in oscillatory microchannel flows: A theoretical and experimental approach," Phys. Fluids **32**, 072008 (2020).
[17]H. Yu, X.-Y. Lu, and H. Huang, "Collective locomotion of two uncoordinated undulatory self-propelled foils," Phys. Fluids **33**, 011904 (2021).
[18]L. Tian, Z. Zhao, W. Wang, and N. Liu, "Length and stiffness effects of the attached flexible plate on the flow over a traveling wavy foil," Acta Mech. Sin. **37**, 1–12 (2021).
[19]P. A. Dewey, B. M. Boschitsch, K. W. Moored, H. A. Stone, and A. J. Smits, "Scaling laws for the thrust production of flexible pitching panels," J. Fluid Mech. **732**, 29 (2013).
[20]M. J. David, R. Govardhan, and J. Arakeri, "Thrust generation from pitching foils with flexible trailing edge flaps," J. Fluid Mech. **828**, 70 (2017).
[21]S. Heathcote and I. Gursul, "Flexible flapping airfoil propulsion at low reynolds numbers," AIAA J. **45**, 1066–1079 (2007).
[22]S. Ramananarivo, R. Godoy-Diana, and B. Thiria, "Rather than resonance, flapping wing flyers may play on aerodynamics to improve performance," Proc. Natl. Acad. Sci. **108**, 5964–5969 (2011).
[23]G.-J. Li and X.-Y. Lu, "Force and power of flapping plates in a fluid," J. Fluid Mech. **712**, 598 (2012).
[24]G. A. Tzezana and K. S. Breuer, "Thrust, drag and wake structure in flapping compliant membrane wings," J. Fluid Mech. **862**, 871–888 (2019).
[25]G. Li, X. Chen, F. Zhou, Y. Liang, Y. Xiao, X. Cao, Z. Zhang, M. Zhang, B. Wu, S. Yin et al., "Self-powered soft robot in the Mariana Trench," Nature **591**, 66–71 (2021).
[26]S. Y. Shinde and J. H. Arakeri, "Flexibility in flapping foil suppresses meandering of induced jet in absence of free stream," J. Fluid Mech. **757**, 231 (2014).
[27]S. Y. Shinde and J. H. Arakeri, "Physics of unsteady thrust and flow generation by a flexible surface flapping in the absence of a free stream," Proc. R. Soc. A: Math. Phys. Eng. Sci. **474**, 20180519 (2018).
[28]J. Alaminos-Quesada and R. Fernandez-Feria, "Propulsion of a foil undergoing a flapping undulatory motion from the impulse theory in the linear potential limit," J. Fluid Mech. **883**, A19 (2020).
[29]M. Kurt, A. Mivehchi, and K. Moored, "High-efficiency can be achieved for non-uniformly flexible pitching hydrofoils via tailored collective interactions," Fluids **6**, 233 (2021).
[30]S. Heathcote and I. Gursul, "Jet switching phenomenon for a periodically plunging airfoil," Phys. Fluids **19**, 027104 (2007).
[31]M. Vanella, T. Fitzgerald, S. Preidikman, E. Balaras, and B. Balachandran, "Influence of flexibility on the aerodynamic performance of a hovering wing," J. Exp. Biol. **212**, 95–105 (2009).
[32]J. D. Eldredge, J. Toomey, and A. Medina, "On the roles of chord-wise flexibility in a flapping wing with hovering kinematics," J. Fluid Mech. **659**, 94–115 (2010).
[33]X. He, Q. Guo, and J. Wang, "Extended flexible trailing-edge on the flow structures of an airfoil at high angle of attack," Exp. Fluids **60**, 1–22 (2019).
[34]W.-X. Huang, S. J. Shin, and H. J. Sung, "Simulation of flexible filaments in a uniform flow by the immersed boundary method," J. Comput. Phys. **226**, 2206–2228 (2007).
[35]J. Ma, Z. Wang, J. Young, J. C. Lai, Y. Sui, and F.-B. Tian, "An immersed boundary-lattice Boltzmann method for fluid-structure interaction problems involving viscoelastic fluids and complex geometries," J. Comput. Phys. **415**, 109487 (2020).
[36]F.-B. Tian, H. Luo, J. Song, and X.-Y. Lu, "Force production and asymmetric deformation of a flexible flapping wing in forward flight," J. Fluids Struct. **36**, 149–161 (2013).
[37]J. Wu, Y. Qiu, C. Shu, and N. Zhao, "Flow control of a circular cylinder by using an attached flexible filament," Phys. Fluids **26**, 103601 (2014).
[38]F.-B. Tian, H. Dai, H. Luo, J. F. Doyle, and B. Rousseau, "Fluid–structure interaction involving large deformations: 3D simulations and applications to biological systems," J. Comput. Phys. **258**, 451–469 (2014).
[39]J. Wu, C. Shu, N. Zhao, and F.-B. Tian, "Numerical study on the power extraction performance of a flapping foil with a flexible tail," Phys. Fluids **27**, 013602 (2015).
[40]J. Deng and C-C. P. Caulfield, "Horizontal locomotion of a vertically flapping oblate spheroid," J. Fluid Mech. **840**, 688–708 (2018).
[41]C. Shu, Y. Wang, C. J. Teo, and J. Wu, "Development of lattice Boltzmann flux solver for simulation of incompressible flows," Adv. Appl. Math. Mech. **6**, 436–460 (2014).
[42]Y. Wang, C. Shu, C. Teo, and J. Wu, "An immersed boundary-lattice Boltzmann flux solver and its applications to fluid–structure interaction problems," J. Fluids Struct. **54**, 440–465 (2015).

[43]X. Zhao, Z. Chen, L. Yang, N. Liu, and C. Shu, "Efficient boundary condition-enforced immersed boundary method for incompressible flows with moving boundaries," J. Comput. Phys. **441**, 110425 (2021).
[44]X. Lin, J. Wu, and T. Zhang, "Self-directed propulsion of an unconstrained flapping swimmer at low Reynolds number: Hydrodynamic behaviour and scaling laws," J. Fluid Mech. **907**, R3 (2021).
[45]D. Kim, J. Cossé, C. Cerdeira, and M. Gharib, "Flapping dynamics of an inverted flag," J. Fluid Mech. **736**, R1 (2013).
[46]C. Zhang, H. Huang, and X.-Y. Lu, "Effect of trailing-edge shape on the self-propulsive performance of heaving flexible plates," J. Fluid Mech. **887**, A7 (2020).
[47]K. Tsuboi and Y. Oshima, "Merging of two dimensional vortices by the discrete vortex method," J. Phys. Soc. Jpn. **54**, 2137–2145 (1985).
[48]T. Karasudani and M. Funakoshi, "Evolution of a vortex street in the far wake of a cylinder," Fluid Dyn. Res. **14**, 331 (1994).
[49]R. Godoy-Diana, C. Marais, J.-L. Aider, and J. E. Wesfreid, "A model for the symmetry breaking of the reverse Bénard-von Kármán vortex street produced by a flapping foil," J. Fluid Mech. **622**, 23 (2009).
[50]Z. C. Zheng and Z. Wei, "Study of mechanisms and factors that influence the formation of vortical wake of a heaving airfoil," Phys. Fluids **24**, 103601 (2012).
[51]C. Marais, B. Thiria, J. E. Wesfreid, and R. Godoy-Diana, "Stabilizing effect of flexibility in the wake of a flapping foil," J. Fluid Mech. **710**, 659–669 (2012).
[52]X. Zhu, G. He, and X. Zhang, "How flexibility affects the wake symmetry properties of a self-propelled plunging foil," J. Fluid Mech. **751**, 164–183 (2014).
[53]Z. Wei and Z. Zheng, "Mechanisms of wake deflection angle change behind a heaving airfoil," J. Fluids Struct. **48**, 1–13 (2014).
[54]X. Zhu, G. He, and X. Zhang, "Flow-mediated interactions between two self-propelled flapping filaments in tandem configuration," Phys. Rev. Lett. **113**, 238105 (2014).
[55]M. S. U. Khalid, J. Wang, H. Dong, and M. Liu, "Flow transitions and mapping for undulating swimmers," Phys. Rev. Fluids **5**, 063104 (2020).
[56]H. Jiang, "Formation mechanism of a secondary vortex street in a cylinder wake," J. Fluid Mech. **915**, A127 (2021).